Author's Accepted Manuscript

# Solution growth of 3D $MnO_2$ mesh comprising 1D nanofibres as a novel sensor for selective and sensitive detection of biomolecules

Bushra Tehseen, Asma Rehman, Muniba Rahmat, Haq Nawaz Bhatti, Aiguo Wu, Faheem K. But, Gul Naz, Waheed S. Khan, Sadia Z. Bajwa

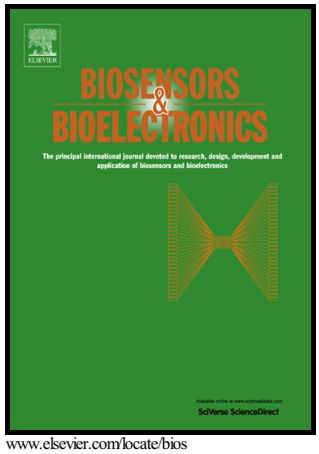


www.elsevier.com/locate/bios

PII: S0956-5663(18)30492-5
DOI: https://doi.org/10.1016/j.bios.2018.06.061
Reference: BIOS10581

To appear in: *Biosensors and Bioelectronic*

Received date: 27 March 2018
Revised date: 11 June 2018
Accepted date: 27 June 2018

Cite this article as: Bushra Tehseen, Asma Rehman, Muniba Rahmat, Haq Nawaz Bhatti, Aiguo Wu, Faheem K. But, Gul Naz, Waheed S. Khan and Sadia Z. Bajwa, Solution growth of 3D $MnO_2$ mesh comprising 1D nanofibres as a novel sensor for selective and sensitive detection of biomolecules, *Biosensors and Bioelectronic,* https://doi.org/10.1016/j.bios.2018.06.061

This is a PDF file of an unedited manuscript that has been accepted for publication. As a service to our customers we are providing this early version of the manuscript. The manuscript will undergo copyediting, typesetting, and review of the resulting galley proof before it is published in its final citable form. Please note that during the production process errors may be discovered which could affect the content, and all legal disclaimers that apply to the journal pertain.

ACCEPTED MANUSCRIPT

# Solution growth of 3D $MnO_2$ mesh comprising 1D nanofibres as a novel sensor for selective and sensitive detection of biomolecules

*Bushra Tehseen*[a,b], *Asma Rehman*[a**], *Muniba Rahmat*[c], *Haq Nawaz Bhatti*[c], *Aiguo Wu*[d], *Faheem K. But*[e], *Gul Naz*[f], *Waheed S. Khan*[a,d***], *Sadia Z. Bajwa*[a*]

[a] *Nanobiotechnology Group, National Institute for Biotechnology and Genetic Engineering (NIBGE), P.O. Box No.577, Jhang Road, Faisalabad, Pakistan*

[b] *Pakistan Institute of Engineering and Applied Sciences, Nilore, Islamabad, Pakistan*

[c] *Department of Chemistry, University of Agriculture, Faisalabad, Pakistan*

[d] *Nanobiomaterials Group, Ningbo Institute of Materials Technology and Engineering (NIMTE), Chinese Academy of Sciences (CAS), Ninbgo City, Zhejiang, China*

[e]*Department of Physics, Division of Science and Technology, University of Education, College Road, Township, Lahore, Pakistan*

[f]*Department of Physics, Faculty of Science, The Islamia University of Bahawalpur, Bahawalpur 63100, Pakistan*

Email: sadya2002pk@yahoo.co.uk

sadia.zafar.bajwa@gmail.com

Email: asmanano@gmail.com

waheedskhan@yahoo.com

*Corresponding Authors Dr Sadia Z. Bajwa Tel: +92-41-2553519 Fax: +92-41-2651472

**Corresponding AuthorsDr Asma Rehman Tel: +92-41-2553519 Fax: +92-41-2651472

***Corresponding AuthorsDr Waheed S. KhanTel: +92-41-2553519 Fax: +92-41-2651472

Accepted manuscript

## Abstract

ACCEPTED MANUSCRIPT

This work is the first report describing the solution grown 3D manganese oxide nanofibrous ($MnO_2$ NFs) mesh and its potential for the simultaneous detection of biomolecules such as ascorbic acid and uric acid. The mesh is synthesized by a facile, one-pot, and cost-effective hydrothermal approach without using any template or structure directing compound. The morphology consists of randomly placed nanofibres possessing a diameter in the range of 10-25 nm, and length of several micron; constituting a highly porous and flexible material. The electrochemical potential was examined by recording cyclic voltammetry signals towards ascorbic acid and uric acid. The special mesh morphology offers a large surface area to promote enhanced electrochemical activity, and also provided a macroporous network that supported efficient mass transport. Additionally, the strong electronic cloud and roughness of $MnO_2$ NFs mesh facilitated the fast oxidation of species at very low potential. The lower detection limit was found to be 1.33 µM (S/N=3) and 1.03 µM (S/N=3) for ascorbic acid and uric acid, respectively. The $MnO_2$ NFs mesh modified electrodes can robustly differentiate both of them by giving well separate signals (Δ=500 mV) indicating capability of the material towards selective detection. The sensor has been successfully applied to human blood and urine samples and the recoveries were found statistically significant. These results demonstrate the practical feasibility of 3D mesh to develop sensors for the accurate diagnosis of clinically important molecules.

**Keywords:** Manganese oxide nanofibrous mesh; Hydrothermal; Electrochemical biosensor; Biomolecules; Cyclic voltammetry

Accepted manuscript

ACCEPTED MANUSCRIPT

## 1. Introduction

Generation of three-dimensional nanomaterials employing one-dimensional structure is recent research attraction due to huge potential in designing innovative technological applications (Gonzalez-Martinez et al., 2016; Patil et al., 2017; Sadhasivam et al., 2017; Shanmugam et al., 2017). Aside from nanotubes, a great amount of various morphological forms such as nanowires and nanorods has been fabricated by using various methods such as laser ablation, templating, arc discharge, vapor-phase transport, and in solution (Chen et al., 2017; Lin et al., 2017; Vandaele et al., 2017; Yeh et al., 2017). All these synthesis strategies are versatile yielding highly pure product, but at the same time are tedious. When it comes to facile synthesis of 1D nanostructures, electrospinning is one of the most popular methods due to its degree of morphological control and a rich variety of materials can be manipulated to produce polycrystalline metal oxide nanostructures.

Recently, much focus has been directed to the preparation of nanowires of the family of oxides, for their exceptional electrical properties. In this regard, several binary oxide nanowires, such as MgO, $SiO_2$, $Ga_2O_3$, $GeO_2$ and ZnO have been reported (Lei et al., 2017; Wang et al., 2017). Among them, transition metal oxides like manganese oxides (MnO) takes precedent owing to outstanding structural, chemical, and physical properties (Bañobre-López et al., 2018; Chinnasamy and Rao 2015; Hou et al., 2014; Meng et al., 2014).

Manganese oxide nanostructures find innovative utility in many fields such as energy storage, dye degradation, bioimaging, biosensing, water oxidation, *etc*. owing to higher charge transfer and increased active surface area (Cakici et al., 2017; Dang et al., 2016; Kuo et al., 2015; Li et al., 2014; Yu et al., 2016; Zhan et al., 2017). Several methods have been reported for the synthesis of nanostructures including lithography, electron beam, electrospinning, template

Accepted manuscript

ACCEPTED MANUSCRIPT

assisted, precipitation method, sol-gel, and electrodeposition (Gonzalez-Martinez et al., 2016; He et al., 2017; Roy et al., 2016; Yang et al., 2016). However, among various synthesis techniques, hydrothermal methods are popular because of simplicity, cost-effectiveness, and versatility (Ma et al., 2004; Wang and Li 2003; Xu et al., 2007).

The determination of ascorbic acid (AA) and uric acid (UA) with high sensitivity is desirable for many clinical diagnosis and food safety applications (Gowthaman et al., 2017; Lv et al., 2017; Zhao et al., 2016). Therefore, low-cost and efficient detection platforms with possibility of clinical diagnostics are highly required. Its significance even increases when already in-vogue analytical methods are cumbersome involving specialized hi-tech equipments (Liu et al., 2017; Zhao et al., 2016).

Now a day, most of the sensing strategies use nanocomposite or hybrid materials based on metal, metal oxide, polymer, or carbon (carbon nanotubes, graphene) for sensing biomolecules and offer improved sensing characteristics by their synergistic effects (Zhang et al., 2016). These composite nanomaterials add cost and it is highly desirable to have facile and direct methods of material fabrication (Bagheri et al., 2017). In this respect, the astounding properties of the 1D nanostructures can be used to develop 3D novel structures; and their surface features can be coupled with electrochemical techniques to develop a sensitive and selective platform for the detection of biomolecules. Previously, some metal/metal oxide NFs meshes have been reported by electrospinning technique, which is expensive, requiring special instruments and expertise (Koo et al., 2016; Singh et al., 2016). Raible and colleagues reported the synthesis of vanadium (V) oxide ($V_2O_5$) NFs mesh using silicon substrate and the fabrication process was carried out for approximately three months to get reasonable length of fibers (Raible et al., 2005).

Accepted manuscript

ACCEPTED MANUSCRIPT

Herein, we report the synthesis of manganese dioxide nanofibrous ($MnO_2$ NFs) mesh by using a one-pot, hydrothermal approach, without using any template. To the best of our knowledge, this is the first report describing the synthesis of metal oxide's NFs mesh by a hydrothermal approach and then exploring its potential for the simultaneous detection of biomolecules. The morphology is exclusively investigated by scanning electron microscope (SEM) whereas, fourier-transform infrared spectroscopy (FT-IR) and dynamic light scattering (DSL) experiments were performed to determine the functionalities of the developed material. Cyclic voltammetry (CV) technique was applied to record the electrochemical signals to manipulate the electrochemical activity of biomolecules. The modified electrodes exhibited superior electrochemical activity and noticeably sharp current peaks for AA and UA determination showing the practical potential of the developed material for clinical diagnostics.

## 2. Experimental

### *2.1. Materials*

All chemicals used in the present work were purchased either from Bio basic Inc. or Sigma Aldrich, and were used as received without any purification. A 50 mM sodium phosphate buffer solution (pH 7.0) was prepared using sodium phosphate monobasic monohydrate and sodium phosphate dibasic heptahydrate. This solution was used as a background medium for the entire electrochemical studies. All solutions were prepared using ultrapure distilled, deionized water ($\rho$ = 18 M$\Omega$ cm) from a Millipore-MilliQ system.

### *2.2. Preparation of $MnO_2$ NFs mesh*

In a typical synthesis, an aqueous solution of manganese acetate tetrahydrate (1 mM) was prepared and stirred for about 10 min at ambient conditions, to ensure homogeneity. In resultant solution, sodium hydroxide (1 M; aqueous solution) was added drop wise with stirring, for



Accepted manuscript

ACCEPTED MANUSCRIPT

another 15 min. As the result, brown color precipitates were formed instantly. Next, the solution was transferred to a Teflon-lined stainless steel autoclave and placed in an oven at 180 °C for 24 hours (optimized conditions), to complete the hydrothermal reaction. To optimize the suitable conditions for the development of monodisperse fibrous morphology, control experiments were also carried out with respect to time (12 and 24 hours) and temperature (25 ± 2 °C and 180 ± 2 °C), keeping all other experimental conditions constant.

After stipulated time, the autoclave was allowed to cool down at room temperature. Finally, it was centrifuged, rinsed with $H_2O$, dried at 60 °C overnight in an oven, and stored in a desiccator at room temperature for further use.

***2.3. Characterization***

The morphology of as the synthesized $MnO_2$ NFs mesh was investigated with field emission scanning electron microscope (FESEM-JSM-7500F-JEOL, Japan). To prepare samples, $MnO_2$ NFs were dispersed in deionized water (1 mg/mL) and 10 μL, out of this dispersion were dropped onto carbon coated copper grids (200 mesh) to obtain images.

Powder X-ray diffraction (P-XRD) spectra of $MnO_2$ NFs were recorded by X'pert Pro PAN analytical (Germany) diffractometer using monochromatic CuKα radiation (λ=1.5406A) operating at 40 kV and current of 30 mA. The data for purity of crystalline structure was collected over a range of 10-80° 2-theta.

Dynamic light scattering (DLS) experiments were carried out to determine the surface potential of $MnO_2$ NFs mesh. For that purpose, a Zeta Sizer (Nano-ZS; Malvern Instruments) with its software, Dispersion Technology Software (DTS) was used.

Fourier-transform infrared spectroscopy (FT-IR) was used to observe the chemical functionalities of the prepared material. For these experiments, a Perkin Elmer System 2000 FT-

Accepted manuscript

ACCEPTED MANUSCRIPT

IR spectrometer in ATR (attenuated total reflection) mode was used. Each sample was assessed in triplicate and 50 scans were averaged for each profile with a spectral resolution of 0.5 $cm^{-1}$. To study optical properties, surface plasmon resonance (SPR) was recorded from 200-700 nm wavelength using a double beam UV/Vis spectrophotometer (CECIL (Aquarius) 7000 series).

### *2.4. Fabrication of $MnO_2$ NFs mesh sensor*

For each study, at least three sensors were prepared by using glassy carbon electrodes (GCE) and before modification, these were cleaned by alumina slurries (1.0, 0.3 and 0.05 µm) followed by their intensive rinsing with 5 mL each of deionized water, nitric acid (1 M) and ethanol. After washing, 10 µL of NFs suspension in water (9 µg/10 µL) was drop-coated over the mirrored surface of GCE electrodes. The resulting layers were then secured with 0.2 µL of Nafion® (10 %). Finally, the electrodes were dried at room temperature overnight and designated as $MnO_2$ NFs mesh sensor.

For the recording of control experiments, bare GCE electrodes were used and all steps were similar, except coatings of NFs mesh layers.

### *2.5. Electrochemical Studies*

The electrochemical responses were observed by recording cyclic voltammetry (CV) signals using a Potentiostat/Galvanostat (Autolab) with a three-electrode system; a glassy carbon electrode modified by the prepared $MnO_2$ NFs mesh as a working electrode, a glassy carbon rod as a counter electrode and a Ag/AgCl electrode as the reference electrode. For all measurements, a sodium phosphate buffer (50 mM) was used as the background medium. Before each experiment, all solutions were degassed with nitrogen (99 %) for 5 min. All CV experiments were carried out at a scan rate of 100 $mVs^{-1}$ (except for investigating the influence of scan rate) and potential range between -1.0 and 1.0 V, at 25 ± 2 °C temperatures.

Accepted manuscript

ACCEPTED MANUSCRIPT

# 3. Results and discussion

### *3.1. Characterization of $MnO_2$ NFs mesh*

The $MnO_2$ NFs mesh is grown by a facile, single-pot, hydrothermal template-free method. The whole process is schematically depicted in Fig. 1A. Initially, in an aqueous solution, ionization occurs (Eq. 1) and metal salt converts into $Mn^{+2}$ and $CH_3COO^-$ ions where, the former reacts with hydroxyl groups present in the water and produces manganese hydroxide ($Mn(OH)_2$; oxidation state II) (Eq. 2).

$$\mathbf{Mn(CH_3COO)_2.4H_2O + H_2O \longrightarrow Mn^{+2} + CH_3COO^- + H^+ + OH^-} \quad \textbf{Eq. (1)}$$

Ionization

$$\mathbf{Mn^{+2} + CH_3COO^- + H^+ + OH^- \longrightarrow Mn(OH)_2 + CH_3COOH + H_2O} \quad \textbf{Eq. (2)}$$

**(soluble/transparent, II oxidation state)**

At this stage, it is still colorless and soluble in appearance like the parent constituents. However, when the alkali (NaOH) is added, it changes to III oxidation state ($Mn(OH)_3$ or $MnO(OH)_2$) (Eq.3). This product is insoluble and brown in color (Wei et al., 2011).

$$\mathbf{Mn(OH)_2 + CH_3COOH + H_2O + NaOH \longrightarrow Mn(OH)_3 / MnO(OH)_2 + CH_3COONa + H_2O}$$

**Eq. (3)**

**(insoluble/brown precipitates, III oxidation state)**

When the hydrothermal treatment occurs under alkaline reaction conditions at elevated temperature, manganese (III) hydroxide converts to manganese (IV) oxide (blackish brown) that builds the nuclei for the growth of nanomaterials (Eq. 4).

$$\mathbf{Mn(OH)_3 / MnO(OH)_2 + H_2O \longrightarrow MnO_2 + H_2O} \quad \textbf{Eq. (4)}$$

**(insoluble/blackish brown)**

Accepted manuscript

ACCEPTED MANUSCRIPT

Next, the solvent, temperature, and the reaction time guide the fabrication of 1D nanostructures (Queraltó et al., 2017; Zhang et al., 2015). These parameters steer the assembling of nanostructures together, which further grow into a specific orientation, developing NFs. Afterwards, their aging at elevated temperature results in the elongation of NFs, generating 3D mesh morphology. In contrast, for control experiments when the only temperature of the reaction was changed (reaction performed at 25 ±2 °C) while keeping all other conditions same. The obtained material showed amorphous morphology with no special geometry after 24 hours (SEM micrograph Fig. S1A). On the other hand, when reaction time was reduced to 12 hours, the resultant material achieved fibrous morphology; however, most of the material possessed rod shapes with different diameters (SEM micrograph is shown in Fig. S1B).

The surface morphology of 3D $MnO_2$ NFs mesh (under optimal conditions; reaction temperature 180 ± 2 °C; reaction time 12 hours) was exclusively investigated by FESEM analysis. Fig. 1 (B, C and D) show the top-view FESEM images of the fibers and mesh. As we can see, these fibers possessed a diameter in the range of 10-25 nm and length was more than 25 µm and the aspect ratio (length to diameter) was calculated to be more than 1000 which in turn confirms their fibrous morphology. Furthermore, these NFs are randomly fashioned in the form of the mesh. This highly porous mesh contained pores ranged from more than 500 nm to less than 1 nm. The SEM micrographs show that the as-prepared material bears very good flexibility, and NFs are making loops and curves smoothly. This mesh structure ensures high connectivity among fibers, therefore we expected improved electrical conductivity which in turn may lead to sensitive electrocatalysis. Several advantages can be taken from this special morphology of the prepared mesh: (1) the 3D structure plays as a great support to offer high specific surface area for interface reaction with enhanced loading and active surface (2) the directly grown mesh prevents

Accepted manuscript

ACCEPTED MANUSCRIPT

the self-aggregation, and provides a free and facile contact both for the electrode and analytes as well (3) the macroporous architecture of the mesh let the molecules conveniently diffuse through the open space to enhance the electrochemical performance.

The surface charge of nanomaterials plays a very decisive role, especially in electrocatalysis. The zeta potential of the $MnO_2$ NFs mesh was studied as and it was found to be -26.3 mV (Fig. 2A). The highly negative surface charge indicates the stability of the formed mesh and further makes it a very favorable support for the fast oxidation of biomolecules (Li et al., 2014). The consumption of chemical functionalities was confirmed by FT-IR analysis to understand the mechanism. Fig. 2B shows the profile of the reaction assembly before hydrothermal reaction (pink line) and final product NFs mesh (blue line) from 4000 to 500 $cm^{-1}$. In the case of reaction mixture, many noticeable bands can be seen. A very broad and intense -OH vibration peak between 3000-4000 showed adsorbed water at the surface, whereas, a band at 740 $cm^{-1}$ represents the OH stretching from metal (Mn-OH), in aqueous solution (Çevik et al., 2016). The bands at 1043 $cm^{-1}$, 1648 $cm^{-1}$, and 2150 $cm^{-1}$ are assigned to the bending vibration of C-O, C-OH, and C-C acetate from metal salt, respectively. If we compare this IR profile with that of the final product, then we can see major changes. All bands of the constituents disappeared and the strong absorption bands emerged at 570 and 690 $cm^{-1}$ which are assigned to the stretching frequencies of Mn-O band. All peaks related to acetate (C-O, C-OH, and C-C) from salt disappeared after hydrothermal process that clearly indicates the formation of pure manganese oxide.

The structural properties of as-prepared $MnO_2$ NFs mesh were examined by XRD measurements and the resultant pattern has been shown in Fig. 2C. The crystalline peaks are assigned to plane (220), (300), (211), (420), (521), (202), and (312) which are consistent with the

Accepted manuscript

ACCEPTED MANUSCRIPT

standard values (JCPDS Card No. 44-0141; Fig. S2). No peaks for amorphous or other types of $MnO_2$ appeared in XRD spectra, suggesting high purity and crystallinity of the final sample (Nawaz et al., 2016; Ristig et al., 2015).

Optical properties of the materials were investigated by recording UV/Vis profile in the range from 200 to 800 and the results are shown in Fig. 2D. It can be seen that the $MnO_2$ exhibited broad absorption bands at 197 to 270 nm and 450 to 785 nm. Therefore, a broader peak is a manifestation of the formation of oxide functionality in the designed $MnO_2$ NFs mesh.

### *3.2. Electrochemical analysis*

The electrochemical properties of $MnO_2$ NFs mesh were studied by the cyclic voltammetry technique. A very fine layer of structures was drop-cast on the surface of GCE and electrochemical responses were observed towards AA. Fig. 3A summarize the outcome of CV experiments when the designed NFs mesh is used towards 10 mM of AA. We observed no redox peaks in the case of bare GCE which indicates poor electron transfer at the interface (black line) of the electrode. In contrast, after functionalization with $MnO_2$ NFs mesh, a very sharp, well-defined oxidation peak was obtained yielding high amount of current *i.e.* 27.1 ± 0.2 µA at 0.27 V (red line; Fig. 3A). Definitely, this high amount of current can be attributed to the presence of $MnO_2$ NFs mesh which conferred electrocatalysis and conductivity reaction sites to support redox reaction. On the other hand, it can also be found that the separation of anodic (0.27 V) and cathodic (0.0 V) peak potentials of $MnO_2$ NFs mesh was calculated to be approximately 270 mV, indicating greatly improved electrode kinetics as well the reversibility of the process. Furthermore, sharpness of the peak suggests strong electronic cloud that generates faradic current, whereas, oxidation at low potential *i.e.* 0.27 V indicates their strong electrocatalytic potential. The higher electrochemical performance of the designed material can be ascribed to 1)

Accepted manuscript

ACCEPTED MANUSCRIPT

NFs mesh morphology with more gaps and pores in-between that results in the enhanced surface area and roughness, offering more binding sites and thus greater interaction with the analyte and; 2) the strong negative zeta potential (-26.3 mV) promoting fast oxidation of species; 3) quantum effects of individual 1D NFs. Here, we cannot forget the role of quantum tunneling towards better performance of the analysis (Li et al., 2014).

To ensure electrochemical potential, we chose another biomolecule which is functional and structural competitor to AA *i.e.* UA. The cyclic voltammograms obtained when bare and $MnO_2$ NFs mesh modified electrode is exposed to 10 mM UA, shown in Fig. 3B. The CV response of bare GCE showed insignificant redox peaks (black line). However, when NFs mesh is used, a prominent oxidation peak (13.2 ± 0.2 µA at 0.67 V; red line) appeared. It validates the electrocatalytic potential of the designed $MnO_2$ NFs mesh. In the case of UA, peak separation was found to be 350 mV (0.67-0.32 V). In conclusion the CV signals of the prepared sensor establish the electrocatalytic potential of the prepared material towards recognizing both biomolecules.

The electrode process was also studied and the influence of scan rate was recorded. Fig. 3C and D displays the resultant CV responses at different scan rates (in the range of 10 to 1000 $mVs^{-1}$) for the oxidation of both AA and UA, respectively. The insets show a corresponding plot of the anodic peak current as a function of the square root of the scan rate ($v^{1/2}$). In both cases, clearly, the oxidation peak current of both biomolecules was gradually increased by increasing the scan rate indicating faster charge transfer kinetics across the modified electrodes. In the case of AA the current was enhanced from 26.6 ± 0.3 µA to 96.2 ± 0.3 µA whereas, for UA it was increased from 2.2 ± 0.1 µA to 24.3 ± 0.1 µA. A linear relationship with a correlation coefficient, $R^2$ = 0.994 and 0.986 for AA and UA, respectively was found. It shows that binding of these

Accepted manuscript

ACCEPTED MANUSCRIPT

molecules within $MnO_2$ NFs mesh was a diffusion controlled process. These results, in turn justify the underlying mechanism by corroborating the diffusion of molecules in the pores of the mesh.

### *3.3. Sensor analytical characteristics*

The CV signals of the designed sensor were also measured against different concentrations of the analytes. We covered a wide range *i.e.* from 0.02 to 10 mM of AA (Fig. 3E) and UA (Fig. 3F). By increasing the concentration of AA, the current increased gradually from 4.1 ± 0.2 µA to 27.1 ± 0.2 µA (linear regression r = 0.998; inset Fig. 3E). The limit of detection (LoD) and limit of quantification (LoQ) were found to be 1.33 µM and 4.0 µM, respectively. We studied an interesting comparison of values with an already reported a study where, $MnO_2$ nanoparticles yielding 10 µM LoD (Luo et al., 2004). The difference of our LoD value from that of the reported strongly validates better performance of our prepared $MnO_2$ NFs mesh as compared to nanoparticles. Undoubtedly, this influence can be attributed to the special fiber based 3D morphology of the mesh which has higher surface with dense electronic clouds that facilitate the fast analysis in electrochemical platform.

In the case of UA, similar to AA, the current increased gradually from 2.6 ± 0.2 µA to 13.2 ± 0.2 µA (linear regression r = 0.986; inset Fig. 3F); LoD and LoQ were found to be 1.03 µM (S/N=3) and 3.17 µM (S/N=3), respectively. Of course, the difference in LoD and LoQ values for AA and UA, with almost same linear range, is due to difference of their electrochemical moieties.

In the chemical structure of AA, electronegative site (oxygen) is not present within the ring that results in the fast oxidation of molecule at low potential yielding higher current than UA whereas, in UA the electronegative element (nitrogen) is present within the ring that requires

Accepted manuscript

ACCEPTED MANUSCRIPT

more potential to oxidize which results in lesser response in the form of peak height (Li et al., 2014).

We compared the linear range and detection limit of our proposed sensor for AA and UA with other published methods; corresponding values are compiled (Table 1). It can be seen that analytical values of our study are more satisfactory than other assorted types of sensors. We believe, this high sensitivity and electrocatalytic activity of our designed sensor can be attributed to the special 3D morphology of $MnO_2$ NFs mesh.

### *3.4. Repeatability and stability*

Repeatability or reproducibility is a very important factor deciding the real life applications of a sensor. Therefore, we prepared 5 different layers of the same quantity of $MnO_2$ NFs mesh over the electrode (each time a fresh one) and exposed to 10 mM AA and UA, separately. All other experimental conditions were kept constant and CV responses were obtained, whereas each individual sensor response was calculated as the average of ten successive scans. The results are summarized in Fig. 4A and B for AA and UA, respectively. It can be seen that electrochemical signals are quite stable. Moreover, about 99 % reproducibility of signals shows the accuracy of the prepared sensors, strongly suggesting suitability of the designed sensor for practical applications.

The stability of the designed sensor was also studied by recoding CVs towards 10 mM, each of AA and UA for five consecutive days on the same modified electrodes at 100 $mVs^{-1}$ scan rate. The results are displayed in Fig. 4C and D for AA and UA, respectively. In the case of both analytes, the current values are statistically almost the same, suggesting the good stability of $MnO_2$ NFs mesh modified GCE. This good stability was ascribed to the special morphology of fiber based 3D mesh. Moreover, the synthesis process offers fabrication of mesh without self-

Accepted manuscript

ACCEPTED MANUSCRIPT

aggregation. This feature ensures better surface coverage of the electrode and thus provision of more number of the binding sites which may have attributed towards good stability.

### *3.5. Selectivity*

Selectivity is a factor of prime importance while deciding the practical applicability. In this respect, we monitored the simultaneous detection of both AA and UA. These analytes have similar functional and structural features, thus can interfere measurements, if found together. We tested $MnO_2$ NFs mesh sensor, to analyze its ability of multiplexing/selective identification in the mixture and CV was performed towards 10 mM, each of AA and UA keeping all other conditions same. The resulting responses are shown in Fig. 5. It can be seen that the modified electrodes show good electrochemical responses for sensing both biomolecules yielding peaks at 27.1 μA at 0.29 V and 13.2 μA at 0.76 V for AA and UA, respectively. When these values are compared with basic sensor signals (Fig. 3A and B), in the case of simultaneous detection almost 82 % and 90 % signal values are analytically generated, regardless these species were found together. It shows that modified electrodes can differentiate well between two species of similar chemical nature with analytical accuracy. The peak separation was calculated to be 500 mV which further validates that the designed 3D $MnO_2$ mesh is capable of differentiating between biomolecules envisaging its potential for clinical applications. When compared with already reported data (Table 1), the selectivity of our designed material was found remarkable. This manifested its strength towards the simultaneous detection of bioanalytes.

### *3.6. Real sample analysis*

To evaluate the applicability of the sensor for the detection of ascorbic acid and uric acid in real samples, blood and urine samples were collected from volunteers healthy human subjects; female (A) and male (B). Sera were separated from blood after 20 minutes of collection. These

Accepted manuscript

ACCEPTED MANUSCRIPT

were centrifuged at 5000 rpm for 20 minutes to remove cell and other clotted materials and afterwards diluted with 50 mM sodium phosphate buffer solution. Urine samples were filtered and diluted with buffer without any other treatment. To assess the reliability of $MnO_2$ NFs mesh sensor known amounts of AA and UA were spiked and a standard addition method was followed. The results are summarized in Table S1. The recoveries of added AA in female blood and urine are 95 % and 117 %, respectively, whereas these values are 108 % and 119 % for male blood and urine samples. However, in the case of UA, the recoveries are 107 % and 104 % in female blood and urine samples and 111 % and 117 % in male blood and urine samples. All the calculated recoveries are good, statistically significant, and in acceptable range between 95 and 119 %. Thus, it can be concluded that our designed sensor based on 3D manganese oxide nanofibrous mesh can determine the presence of AA and UA in real samples by using an external calibration curve.

## 4. Conclusion

To enhance the sensitivity and selectivity for the determination of biomolecules, 3D manganese oxide nanofibrous mesh was grown by one-pot, hydrothermal, and template-free approach. 1D nanofibres possessed 10-25 nm diameter and randomly arranged in a 3D mesh fashion. This morphology ensured larger surface area and quantum effects, whereas overall 3D mesh structure with interconnected pores (500 nm to less than 1 nm) and voids facilitated enhanced diffusion of biomolecules and electrochemical performance. The prepared mesh generated good electrochemical signals in the presence of ascorbic acid and uric acid, yielding LoD of 1.33 and 1.03 µM, respectively. Remarkably, the sensor showed well-separated voltammetric peaks with 500 mV potential difference in simultaneous detection. This work

Accepted manuscript

ACCEPTED MANUSCRIPT

paves the way to design nanomaterials with exciting 3D morphologies to develop sensitive and selective sensor for the detection of clinically important molecules.

## Acknowledgement

The authors are thankful to the International Foundation for Science (IFS) for funding this study via research project no W/5571-1, co-funded by the Organization for the Prohibition of Chemical Weapons (OPCW), The Hague; and project no. E-5659, co-funded by the Organization of Islamic Cooperation's (OIC) Standing Committee on Scientific and Technological Cooperation (COMSTECH), Islamabad.

## Notes

The authors declare no competing financial interest.

## Novelty Statement

In this study, we have introduced a facile, one-pot method for solution based growth of 3D $MnO_2$ nanofibrous mesh for electrochemical sensitive detection of ascorbic acid and uric acid. The morphology holds many special features such as catalytic capability of nanostructured $MnO_2$, fibrous 1D structure offering more surface area and quantum effect, and overall 3D mesh morphology with mesoporous characteristics yielding interconnected pores and spaces for enhanced diffusion and electrochemical performance. This sensor design delivers both superior sensitivity and specificity. This is the first time such structures are being reported for bio-analytes detection.

Accepted manuscript

ACCEPTED MANUSCRIPT

## References

Bagheri, H., Pajooheshpour, N., Jamali, B., Amidi, S., Hajian, A., Khoshsafar, H., 2017. Microchem. J. 131, 120-129.

Bañobre-López, M., García-Hevia, L., Cerqueira, M.F., Rivadulla, F., Gallo, J., 2018. Chem. Eur. J. 24, 1295-1303.

Cakici, M., Kakarla, R.R., Alonso-Marroquin, F., 2017. Chem. Eng. J. 309, 151-158.

Çevik, S., Akpolat, O., Anik, Ü., 2016. Food Anal. Methods. 9, 500-504.

Chen, M., Zou, Y., Wu, L., Pan, Q., Yang, D., Hu, H., Tan, Y., Zhong, Q., Xu, Y., Liu, H., 2017. Adv. Funct. Mater. 27, 1-7.

Chinnasamy, R., Rao, G.M., 2015. Mater. Sci. Semicond. Process. 31, 709-714.

Dang, T.D., Banerjee, A.N., Tran, Q.T., Roy, S., 2016. J. Phys. Chem. Solids. 98, 50-58.

Gonzalez-Martinez, I., Bachmatiuk, A., Bezugly, V., Kunstmann, J., Gemming, T., Liu, Z., Cuniberti, G., Rümmeli, M., 2016. Nanoscale. 8, 11340-11362.

Gowthaman, N., Sinduja, B., Karthikeyan, R., Rubini, K., John, S.A., 2017. Biosens. Bioelectron. 94, 30-38.

He, Q., Tan, C., Zhang, H., 2017. ACS Nano. 11, 4381-4386.

Hou, C., Liu, H., Zhang, D., Yang, C., Zhang, M., 2016a. J. Alloys.Compd. 666, 178-184.

Hou, J., Li, Y., Mao, M., Ren, L., Zhao, X., 2014. ACS Appl. Mater. Interfaces. 6, 14981-14987.

Hou, T., Gai, P., Song, M., Zhang, S., Li, F., 2016b. J. Mater. Chem. B. 4, 2314-2321.

Koo, W.T., Choi, S.J., Kim, S.J., Jang, J.S., Tuller, H.L., Kim, I.D., 2016. J. Am. Chem. Soc. 138, 13431-13437.

Kuo, C.H., Mosa, I.M., Poyraz, A.S., Biswas, S., El-Sawy, A.M., Song, W., Luo, Z., Chen, S.Y., Rusling, J.F., He, J., 2015. ACS Catal. 5, 1693-1699.

Accepted manuscript

ACCEPTED MANUSCRIPT

Lamari, A.S., El Fattouh, A., El Qouatli, S.E., Najih, R., Chtaini, A., 2013. Res. Rev. Polym. 4, 32-36.

Lei, D., Benson, J., Magasinski, A., Berdichevsky, G., Yushin, G., 2017. Science 355, 267-271.

Li, M., Guo, W., Li, H., Dai, W., Yang, B., 2014. Sens. Actuators B: Chem. 204, 629-636.

Li, N., Diao, W., Han, Y., Pan, W., Zhang, T., Tang, B., 2014. Chem. Eur. J. 20, 16488-16491.

Lin, K., Yao, P., Zhao, J., Guo, S., Tian, F., 2017. Mater. Lett. 203, 21-23.

Liu, Y., Li, H., Guo, B., Wei, L., Chen, B., Zhang, Y., 2017. Biosens. Bioelectron. 91, 734-740.

Luo, X.L., Xu, J.J., Zhao, W., Chen, H.Y., 2004. Anal. Chim. Acta. 512, 57-61.

Lv, S., Zhang, K., Lin, Z., Tang, D., 2017. Biosens. Bioelectron. 96, 317-323.

Ma, R., Bando, Y., Zhang, L., Sasaki, T., 2004. Adv. Mater. 16, 918-922.

Meng, Y., Song, W., Huang, H., Ren, Z., Chen, S.-Y., Suib, S.L., 2014. J. Am. Chem. Soc. 136, 11452-11464.

Nawaz, F., Xie, Y., Xiao, J., Cao, H., Ghazi, Z.A., Guo, Z., Chen, Y., 2016. Catal. Sci. Technol. 6, 7875-7884.

Ngai, K.S., Tan, W.T., Zainal, Z., Zawawi, R.M., Zidan, M., 2013. Int. J. Electrochem. Sci. 8, 10557-10567.

Patil, J.V., Mali, S.S., Kamble, A.S., Hong, C.K., Kim, J.H., Patil, P.S., 2017. Appl. Surf. Sci. 423, 641-674.

Queraltó, A., de la Mata, M., Arbiol, J., Hühne, R., Obradors, X., Puig, T., 2017. Cryst. Growth Des. 17, 504-516.

Raible, I., Burghard, M., Schlecht, U., Yasuda, A., Vossmeyer, T., 2005. Sens. Actuators B: Chem. 106, 730-735.

Ristig, S., Cibura, N., Strunk, J., 2015. Green. 5, 23-41.

Accepted manuscript

ACCEPTED MANUSCRIPT

Roy, M., Basak, S., Naskar, M.K., 2016. Phys. Chem. Chem. Phys. 18, 5253-5263.

Sadhasivam, T., Kim, H.T., Jung, S., Roh, S.H., Park, J.H., Jung, H.Y., 2017. Renew Sustaina Energy Rev. 72, 523-534.

Shanmugam, N., Muthukumar, S., Prasad, S., 2017. Anal. Methods. 9, 5525-5533.

Singh, G., Vanangamudi, A., Prince, J.A., 2016. US Patents. 9,421,293.

Vandaele, K., Heremans, J., Van Driessche, I., Van Der Voort, P., De Buysser, K., 2017. Chem. Commun. 53, 12294-12297.

Wang, H., Zhang, Y., Wang, Y., Ma, H., Du, B., Wei, Q., 2017. Biosens. Bioelectron. 87, 745-751.

Wang, X., Li, Y., 2003. Chem. Eur. J. 9, 300-306.

Wei, W., Cui, X., Chen, W., Ivey, D.G., 2011. Chem. Soc. Rev. 40, 1697-1721.

Xu, M., Kong, L., Zhou, W., Li, H., 2007. J. Phys. Chem. C. 111, 19141-19147.

Yang, G., Wang, L., Wang, J., Wei, W., Yan, W., 2016. Mater. Des. 112, 429-435.

Yeh, Y.W., Raitses, Y., Koel, B.E., Yao, N., 2017. Sci. Rep. 7, 3075.

Yu, G., Zhao, Q., Wu, W., Wei, X., Lu, Q., 2016. Talanta 146, 707-713.

Zhan, Y., Shi, S., Ehlerding, E.B., Graves, S.A., Goel, S., Engle, J.W., Liang, J., Tian, J., Cai, W., 2017. ACS Appl. Mater. Interface. 9, 38304-38312.

Zhang, L., Feng, J., Chou, K.-C., Su, L., Hou, X., 2017. J. Electroanal. Chem. 803, 11-18.

Zhang, X., Zhang, Y.C., Ma, L.X., 2016. Sens. Actuators B: Chem. 227, 488-496.

Zhang, Z., Lv, Y., Yan, J., Hui, D., Yun, J., Zhai, C., Zhao, W., 2015. J. Alloys Compd. 650, 374-380.

Zhao, D., Yu, G., Tian, K., Xu, C., 2016. Biosens. Bioelectron. 82, 119-126.

Accepted manuscript

ACCEPTED MANUSCRIPT

Accepted manuscript

## List of Figures

ACCEPTED MANUSCRIPT

prepared $MnO_2$ NFs mesh **(C)** XRD pattern of the as prepared $MnO_2$ NFs mesh **(D)** UV visible spectra of $MnO_2$ NFs mesh.

**Fig. 3** **Sensor Characteristics;** Cyclic voltammograms obtained with bare and $MnO_2$ NFs mesh electrode surface responses towards 10 mM of **(A)** ascorbic acid and **(B)** uric acid; scan rate 100 $mVs^{-1}$**.** Cyclic voltammograms showing the influence of scan rate towards 10 mM of **(C)** ascorbic acid and **(D)** uric acid; scan range 10-1000 $mVs^{-1,}$ inset shows respective regression plots. Cyclic voltammograms showing the influence of increasing concentration of **(E)** ascorbic acid and **(F)** uric acid from 0.02 to 10 mM, inset shows respective regression plots. In all these electrochemical studies, sodium phosphate buffer (50 mM) was used as the background medium.

**Fig. 4** **Sensor parameters;** the reproducibility data of the $MnO_2$ NFs mesh sensor towards 10 mM of **(A)** ascorbic acid and **(B)** uric acid. Stability profile of $MnO_2$ NFs mesh for 10 mM of **(C)** ascorbic acid and **(D)** uric acid. For all these experiments reaction conditions are; 50 mM sodium phosphate was used as background medium, scan rate 100 $mVs^{-1}$**.**

**Fig. 5** **Selectivity profile**: Cyclic voltammograms of $MnO_2$ NFs mesh towards 10 mM each of ascorbic acid and uric acid; For this reaction sodium phosphate buffer (50 mM) was used as the background medium.

Accepted manuscript

ACCEPTED MANUSCRIPT

Accepted manuscript

**Graphical Abstract**

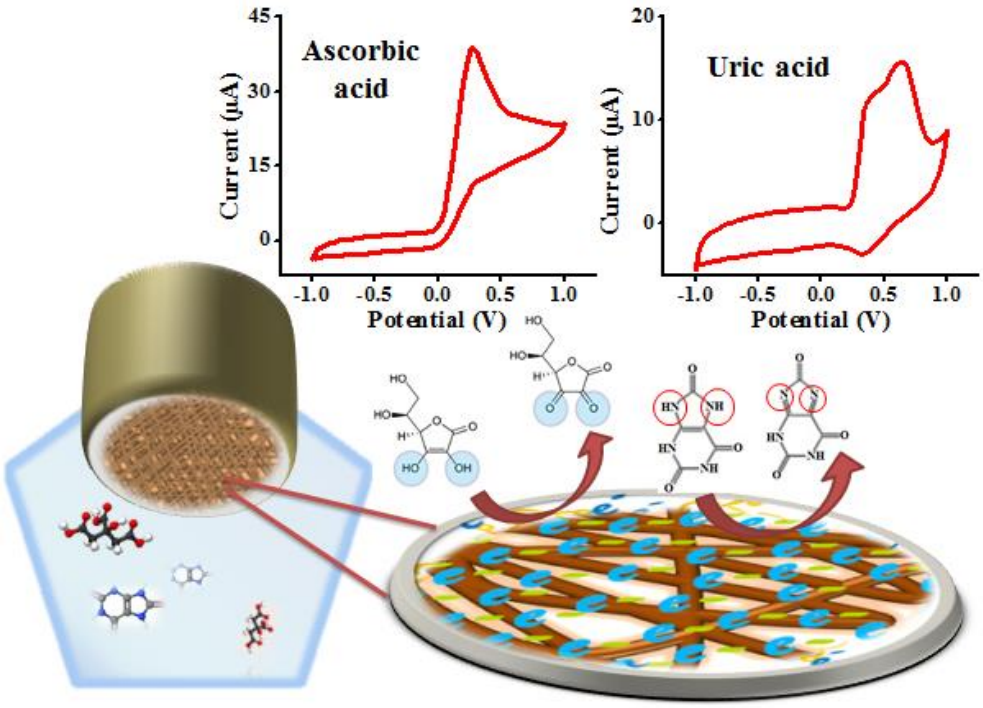


**Fig. 1**

Accepted manuscript

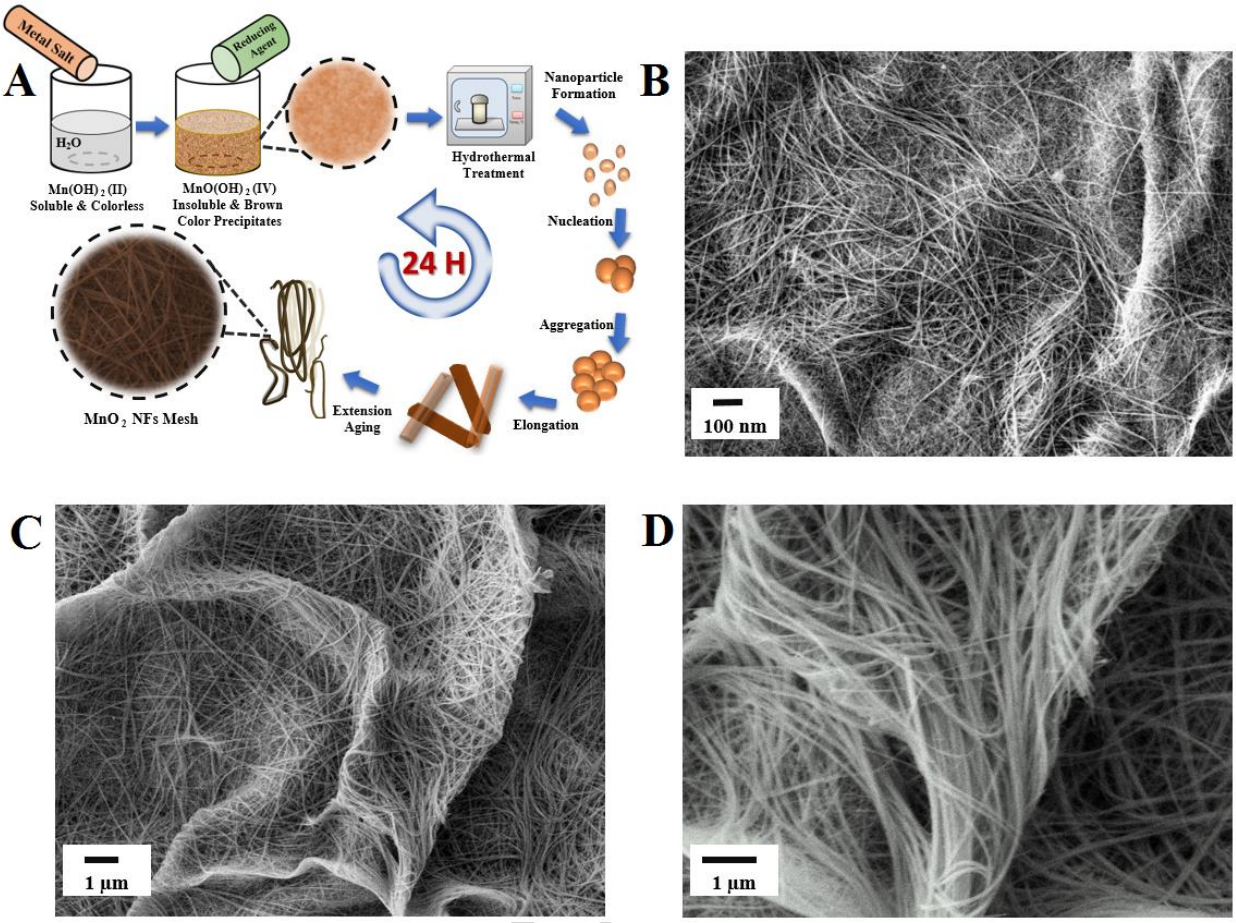


Accepted

**Fig. 2**

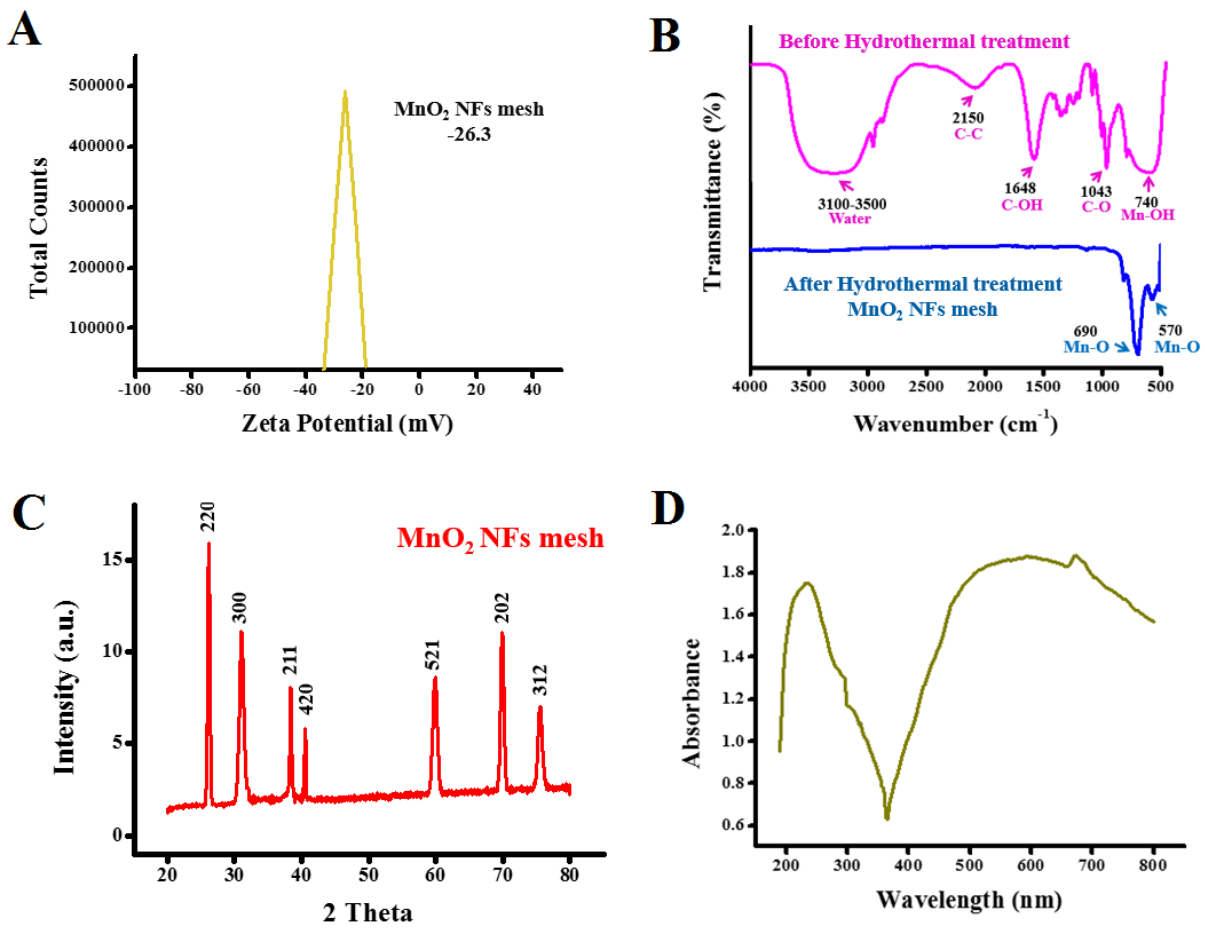


Accepted

**Fig. 3**

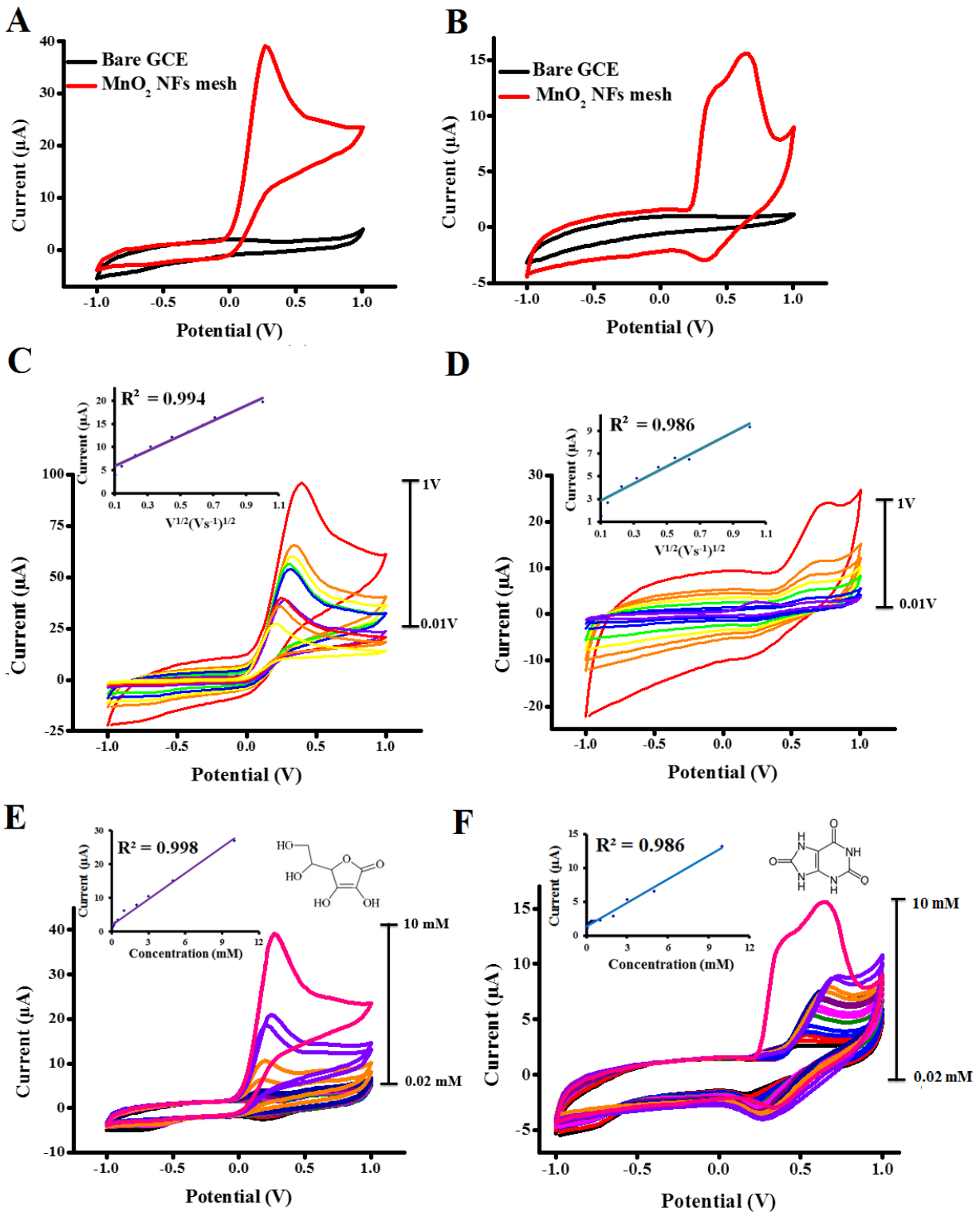
A
Bare GCE
MnO2 NFs mesh
Current (μA)
Potential (V)
B
Bare GCE
MnO2 NFs mesh
Current (μA)
Potential (V)
C
R² = 0.994
Current (μA)
V1/2(Vs-1)1/2
1V
0.01V
Current (μA)
Potential (V)
D
R² = 0.986
Current (μA)
V1/2(Vs-1)1/2
1V
0.01V
Current (μA)
Potential (V)
E
R² = 0.998
Current (μA)
Concentration (mM)
10 mM
0.02 mM
Current (μA)
Potential (V)
F
R² = 0.986
Current (μA)
Concentration (mM)
10 mM
0.02 mM
Current (μA)
Potential (V)

**Fig. 4**

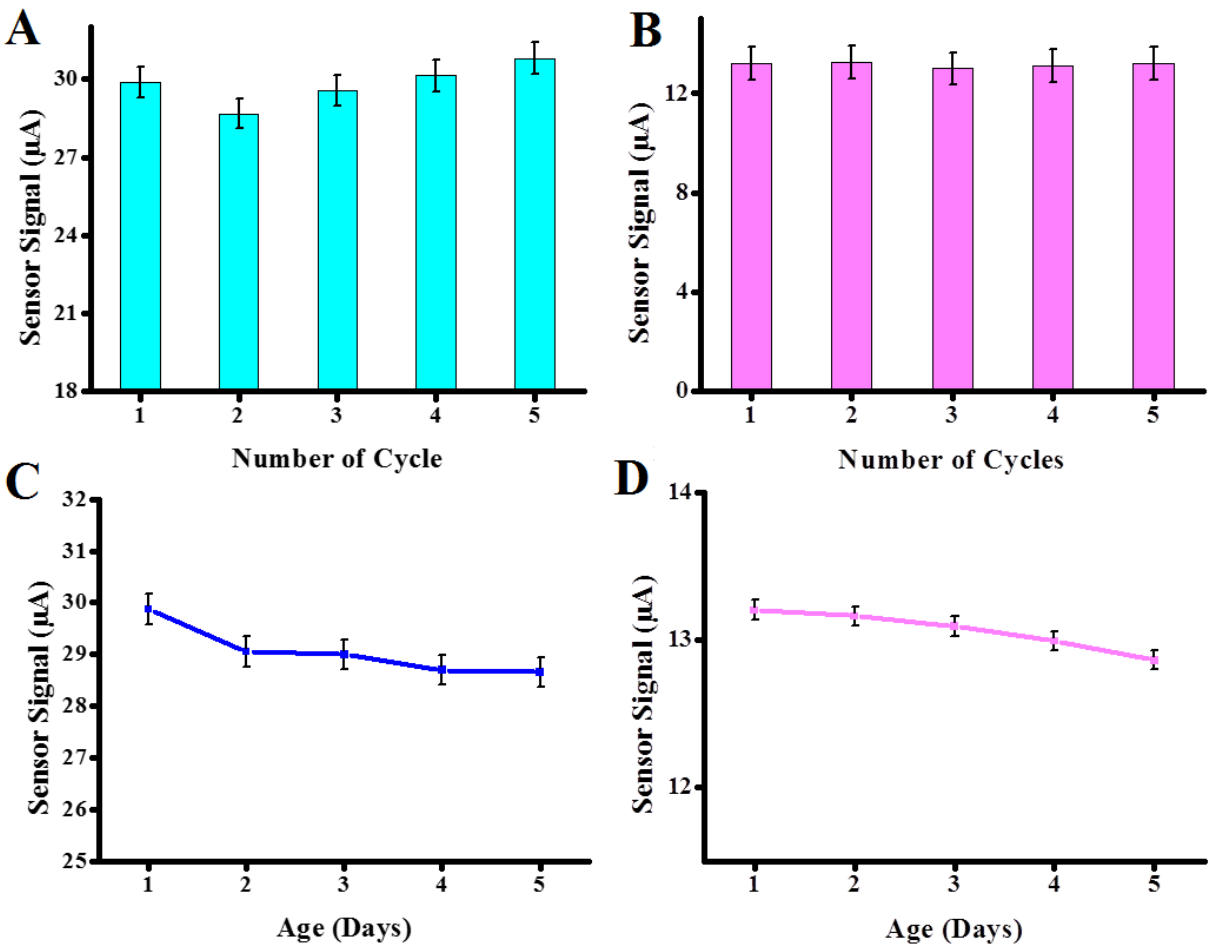


Accepted

**Fig. 5**

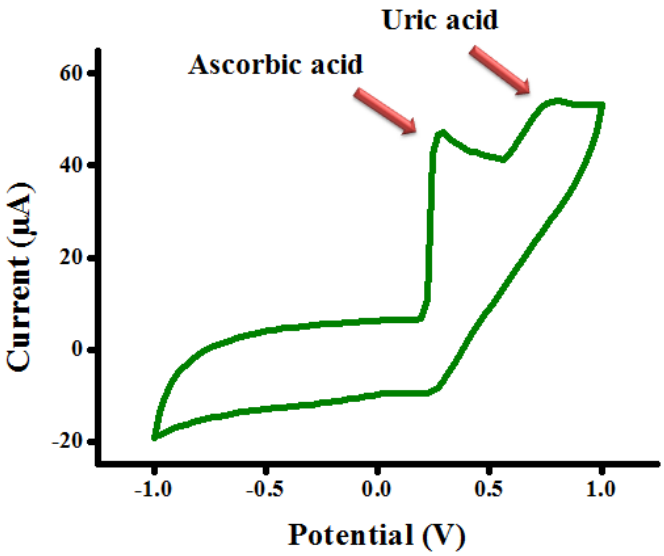


Accepted manuscript

ACCEPTED MANUSCRIPT

**Table 1.** Comparison of sensor analytical parameters with already reported methods for the detection of ascorbic acid and uric acid.

| **Analyte** | **Electrode** | **Method** | **Linear range (mM)** | **LoD (μM)** | **Selectivity** | **Reference** |
|---|---|---|---|---|---|---|
| AA | SWCNT/ZnO/GCE | CV | 0.2-10 | 85 | Only one analyte (AA) was studied in this work | (Ngai et al., 2013) |
| AA | HNP-PtTi/GCE | CV | 0.2-1.0 | 24.2 | AA and UA peak separation is 345 mV | (Zhao et al., 2016) |
| AA | $SiO_2$@AuNPs@PANI/CS/GCE | CV | 0-1.2 | 6 | AA and UA peak separation is 384 mV | (Hou et al., 2016b) |
| AA | Carbon paste electrode | CV | 0.2-9 | 5.48 | Only one analyte (AA) was studied in this work | (Lamari et al., 2013) |
| AA and UA | RGO–ZnO/GCE | DPV | AA 0.05-2.53 UA 0.003-0.33 | AA 3.71 UA 1.08 | AA and UA peak separation is 368 mV | (Zhang et al., 2016) |

Accepted manuscript

ACCEPTED MANUSCRIPT

| | | | | | | |
|---|---|---|---|---|---|---|
| AA | CL-TiN/GCE) | DPV | 0.05-1.5 | 1.52 | AA and UA peak separation is 190 mV | (Zhang et al., 2017) |
| AA and UA | ZnO-Au/GCE | DPV | AA 0.1-4 UA 0.01-0.4 | AA 4.699 UA 2.337 | AA and UA peak separation is 226 mV | (Hou et al., 2016a) |
| AA and UA | $MnO_2$ NF/GCE | CV | 0.02-10 | AA 1.33 UA 1.03 | AA and UA peak separation is 500 mV | This work |

Accepted manuscript

ACCEPTED MANUSCRIPT

# Supplementary Information

## Fig. S1

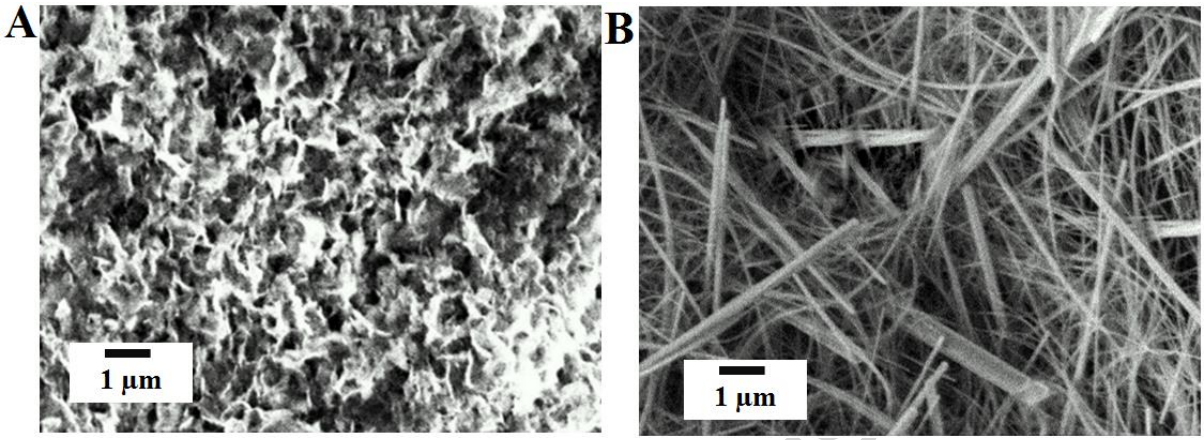


**Fig. S1: Control experiment; (A)** SEM image of control experiment at 25 ± 2 °C; 24 hours **(B)** SEM image of control experiment at 180 ± 2 °C; 12 hours

Accepted manuscript

ACCEPTED MANUSCRIPT

**Fig. S2**

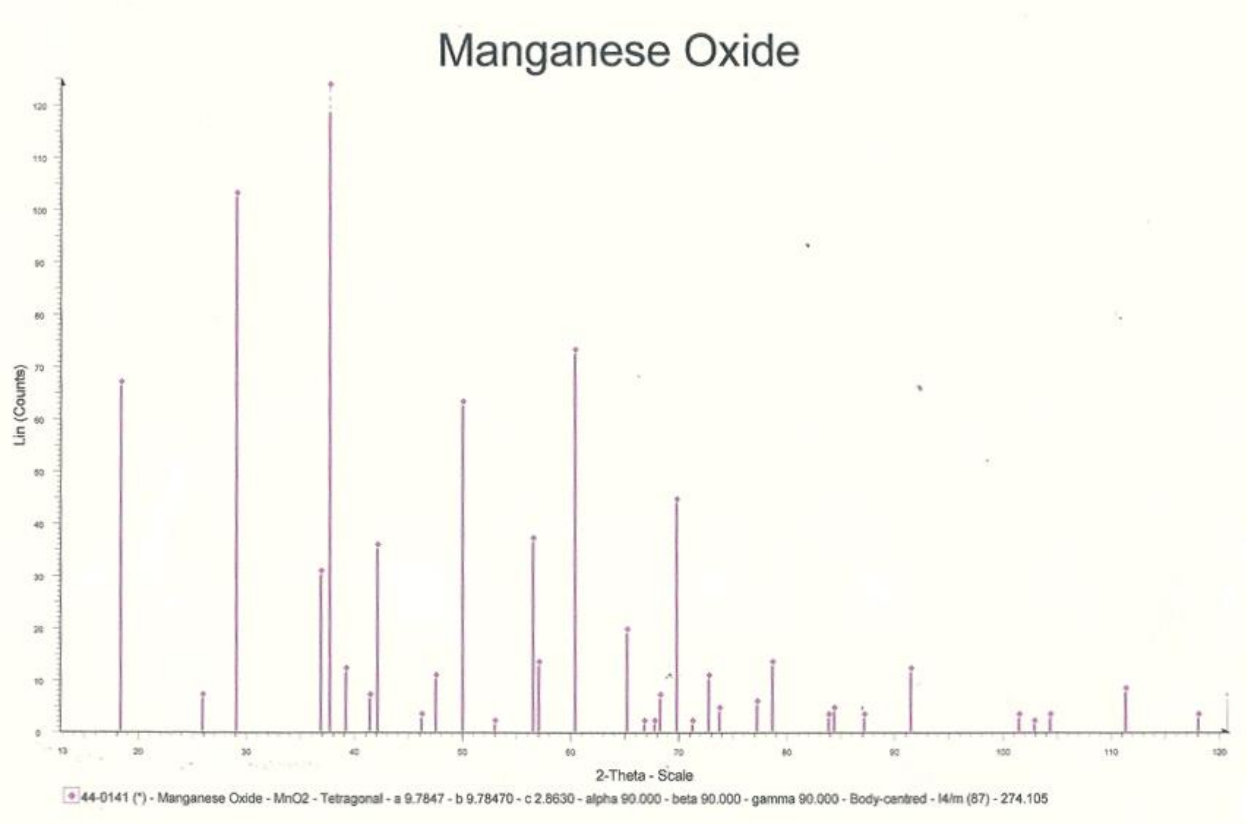


**Fig. S2:** Standard JCPDS card 44-0141 for manganese oxide

Accepted

**Fig. S3**

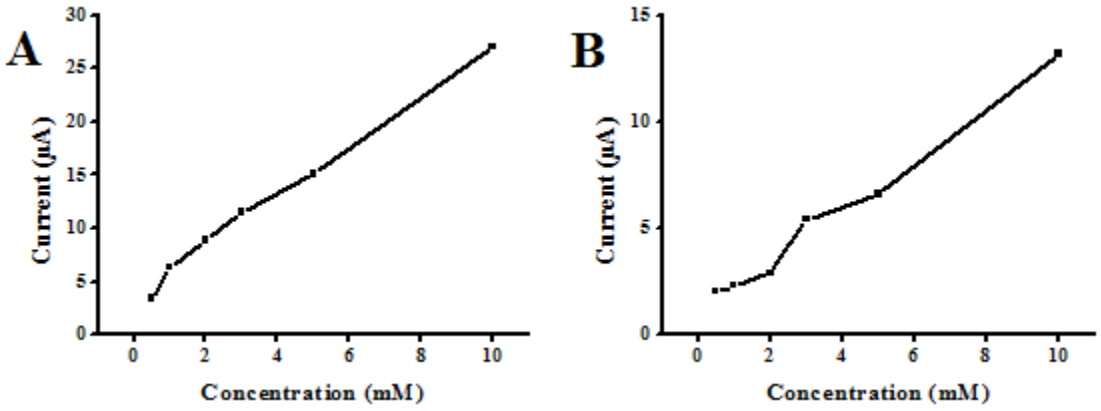


**Fig. S3:** Linear relationship between concentration and current response **(A)** ascorbic acid; **(B)** uric acid.

Accepted manuscript

ACCEPTED MANUSCRIPT

Table S1: Determination of ascorbic acid and uric acid in human blood and urine samples

| Analyte | Sample | Blood Serum | | Recovery* (%) | Average (%) | Urine | | Recovery* (%) | Average (%) |
|---|---|---|---|---|---|---|---|---|---|
| | | Added (mM) | Found* (mM) | | | Added (mM) | Found* (mM) | | |
| **Ascorbic acid** | **A** | 0.01 | 0.009 ± 0.0005 | 93.3 ± 5.7 | 95.4 ± 2.36 | 0.01 | 0.013 ± 0.002 | 133.3 ± 28.87 | 116.7 ± 15.51 |
| | | 0.1 | 0.095 ± .005 | 95 ± 5 | | 0.1 | 0.114± 0.013 | 114 ± 31.3 | |
| | | 0.5 | 0.49 ± 0.005 | 98.6 ± 1.1 | | 0.5 | 0.513 ± 0.023 | 102.7 ± 6.4 | |
| | **B** | 0.01 | 0.011 ± 0.001 | 113.3 ± 11.5 | 107.8 ± 5.6 | 0.01 | 0.012 ± 0.0028 | 120 ± 26.6 | 118.6 ± 2.2 |
| | | 0.1 | 0.108 ± 0.012 | 108 ± 12 | | 0.1 | 0.119 ± 0.026 | 119.7 ± 26.84 | |
| | | 0.5 | 0.51± 0.017 | 102 ± 12 | | 0.5 | 0.58± 0.026 | 116 ± 5.2 | |
| **Uric acid** | **A** | 0.01 | 0.01 ± 0.0015 | 103.33 ± 15 | 107.44 ± 3.5 | 0.01 | 0.011 ± 0.001 | 116.7 ± 15.28 | 104.9 ± 10.25 |
| | | 0.1 | 0.109 ± 0.034 | 109.6 ± 34.9 | | 0.1 | 0.1 ± 0.01 | 100 ± 17.3 | |
| | | 0.5 | 0.546 ± 0.035 | 109.3 ± 7.02 | | 0.5 | 0.49 ± 0.01 | 98 ± 2 | |
| | **B** | 0.01 | 0.012 ± 0.0025 | 123.33 ± 25.16 | 111.20 ± 11.8 | 0.01 | 0.013 ± 0.001 | 136.7 ± 15.2 | 117.3 ± 17 |
| | | 0.1 | 0.099 ± 0.015 | 99.6 ± 15.5 | | 0.1 | 0.11 ± 0.01 | 110 ± 10 | |
| | | 0.5 | 0.553± 0.065 | 110.6± 13.01 | | 0.5 | 0.52± 0.025 | 105.3 ± 5.03 | |

* Mean value of three determinations

Accepted manuscript

ACCEPTED MANUSCRIPT

# Research Highlights

- This is the first report about the synthesis of 3D $MnO_2$ nanofibrous mesh by a simple, one-pot hydrothermal approach for the electrochemical detection of ascorbic acid and uric acid.
- $MnO_2$ fibers possessed a diameter in the range of 10-25 nm and length of several micron, arranged randomly in a 3D mesh fashion.
- The mesh consists of pores ranged from more than 500 nm to less than 1 nm facilitating enhanced diffusion which widely improves sensitivity and selectivity.

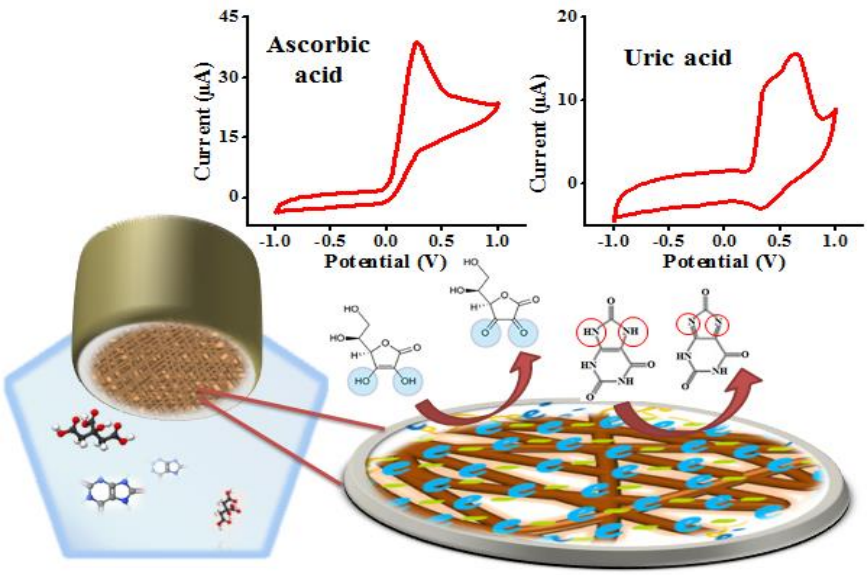

ACCEPTED MANUSCRIPT

Accepted manuscript